Downloaded via PENNSYLVANIA STATE UNIV on April 6, 2023 at 19:58:40 (UTC). See https://pubs.acs.org/sharingguidelines for options on how to legitimately share published articles.



www.acsnano.org

# Toward a Mechanistic Understanding of the Formation of 2D-GaN<sub>x</sub> in Epitaxial Graphene

Anushka Bansal, Nadire Nayir, Ke Wang, Patrick Rondomanski, Shruti Subramanian, Shalini Kumari, Joshua A. Robinson, Adri C. T. van Duin, and Joan M. Redwing\*



Cite This: ACS Nano 2023, 17, 230-239



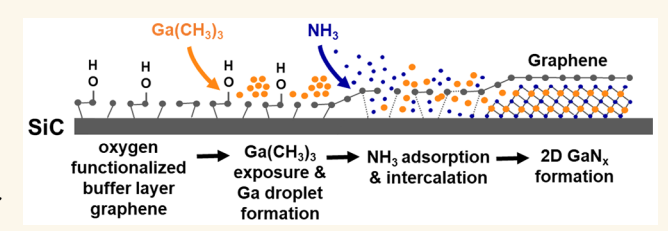
ACCESS I

III Metrics & More

Article Recommendations

s Supporting Information

ABSTRACT: Ultrathin 2D-GaN $_x$  can be formed by Ga intercalation into epitaxial graphene (EG) on SiC followed by nitridation in ammonia. Defects in the graphene provide routes for intercalation, but the nature and role of the defects have remained elusive. Here we examine the influence of graphene layer thickness and chemical functionalization on Ga intercalation and 2D-GaN $_x$  formation using a combination of experimental and theoretical studies. Thin buffer layer regions



of graphene near steps on SiC readily undergo oxygen functionalization when exposed to air or a  $He/O_2$  plasma in contrast to thicker regions which are not chemically modified. Oxygen functionalization is found to inhibit Ga intercalation leading to accumulation of Ga droplets on the surface. In contrast, Ga readily intercalates between EG and SiC in the thicker graphene regions that do not contain oxygen. When  $NH_3$  annealing is carried out immediately after Ga exposure, 2D- $GaN_x$  formation is observed only in the oxygen-functionalized regions, and Ga intercalated under thicker nonfunctionalized graphene does not convert to  $GaN_x$ . Density functional theory calculations demonstrate that oxygen functionalization of graphene alters the binding energy of Ga and  $NH_3$  species to the graphene surface. The presence of hydroxyl groups on graphene inhibits binding of Ga to the surface; however, it enhances the chemical reactivity of the graphene surface to  $NH_3$  which, in turn, enhances Ga binding and facilitates the formation of 2D- $GaN_x$ . By modifying the EG process to produce oxygen-functionalized buffer layer graphene, uniformly intercalated 2D- $GaN_x$  is obtained across the entire substrate surface.

KEYWORDS: epitaxial graphene, 2D materials, GaN, metalorganic chemical vapor deposition, defects, intercalation

ollowing the discovery of graphene, two-dimensional (2D) materials have garnered interest among researchers due to their intriguing properties and potential for practical applications. The electronic properties of 2D materials vary from "semimetal" graphene to "semiconducting" transition metal chalcogenides (TMDs) and "insulating" hexagonal boron nitride (hBN). <sup>1-3</sup> Moreover, 2D forms of III-V nitrides such as GaN, AlN, and InN are predicted to have substantially different properties from their bulk 3D counterparts.<sup>4-7</sup> However, experimental realization of such 2D counterparts is difficult because obtaining atomically thin layers by cleaving tetrahedrally coordinated bulk crystals results in unsaturated dangling bonds on the surface. Al Balushi et al. experimentally discovered a pathway to artificially stabilize a 2D form of GaN by encapsulating it between epitaxial graphene (EG) and SiC.9 Using metalorganic chemical vapor deposition (MOCVD), gallium adatoms were delivered to the EG surface using trimethylgallium (TMGa) as a precursor, penetrated between EG and the SiC substrate, and were converted into 2D-GaN<sub>r</sub> via exposure to ammonia (NH<sub>3</sub>) at moderate temperatures. 2D-GaN<sub>x</sub> synthesized in this case has a 2:3 stoichiometry (space group: R3m) as compared to wurtzite

GaN with a stoichiometry of 1:1 (space group:  $P6_3mc$ ). <sup>10</sup> 2D-GaN<sub>x</sub> exhibits covalent bonding to the SiC substrate while preserving a van der Waals (vdW) gap with graphene. There are also other reports of 2D-GaN and 2D AlN synthesis by MOCVD via successful intercalation between transferred CVD graphene and Si(111) using TMGa and trimethyl aluminum (TMAl) as metal sources and NH<sub>3</sub> as a source of N. <sup>11,12</sup> The formation of 2D InN was also achieved via intercalation of indium and N between EG and SiC substrate using MOCVD. <sup>13</sup> Briggs et al. also successfully synthesized atomically thin metals such as Ga, In, and Sn which are promising materials for nanophotonics and plasmonics due to their nonlinear optical properties, using a thermal evaporation process described as confinement heteroepitaxy (CHet). <sup>14–16</sup>

Received: July 17, 2022
Accepted: December 22, 2022
Published: December 29, 2022





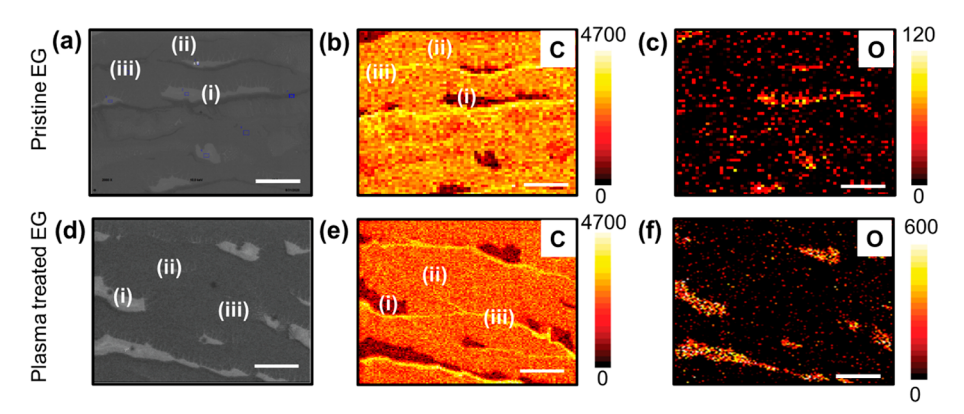


Figure 1. (a) SEM image of as-grown EG where different contrast corresponds to variations in graphene layer thickness; bright contrast corresponds to thinner EG (i), whereas dark contrast represents thicker EG (ii), and the thickest EG is at the step edges (iii). (b, c) C and O maps, respectively, of the as-received EG sample demonstrating the presence of more C-O bonds/oxygen functionalization in regions of thinner graphene. In the case of plasma-treated EG, the SEM image (d) shows similar differences in contrast while the spatial distribution of C-O bonds is confirmed by AES mapping of C (e) and O (f) across the region. Note the increased scale bar in panel f compared to that in panel c, indicating an increase in O intensity in the thinner graphene regions post-plasma-treatment compared to as-received. The scale bar on the SEM and AES images is  $10 \ \mu m$ .

In multiple studies mentioned above, it was found that atomic vacancies/defects in graphene facilitate the intercalation process allowing increased lateral coverage of intercalant at the EG/SiC interface, which is otherwise limited in spatial distribution across the substrate. By intentionally creating defects in EG using plasma treatment, Briggs et al. reported >10 µm intercalated regions of 2D-Ga between graphene and SiC using metallic Ga as a precursor. 15 Al Balushi et al. using TMGa reported  $\sim 1-2 \mu m$  patches of 2D-GaN<sub>x</sub> intercalated between graphene and SiC.9 Even though defects in the graphene layer are effective to enhance intercalation, the nature of the defects and their impact on intercalation and chemical conversion of intercalants has remained elusive. Two recent studies using reactive force fields (ReaxFF) and density functional theory (DFT)<sup>17,18</sup> show that Ga intercalation through mono- and divacancies is kinetically hindered while larger size defects (>divacancy) significantly lower the kinetic barrier encountered during Ga penetration through graphene and, by consequence, lower the growth temperature required for the 2D-Ga fabrication.

EG is commonly produced by heating Si-face SiC substrates to temperatures above 1200 °C under ultrahigh vacuum which results in the sublimation of Si atoms from the (0001) SiC surface and subsequent  $(6\sqrt{3} \times 6\sqrt{3})$  R30° reconstruction of the remaining carbon atoms. <sup>19</sup> The reconstructed carbon layer is commonly referred to as the buffer layer (BL) and consists of carbon atoms in a honeycomb structure, a portion of which are covalently bound to Si in the underlying SiC. Depending on conditions used for the EG formation, additional layers including single layer (SL) and multilayer graphene can be present on top of the BL giving rise to an EG surface of varying thicknesses. Previous studies have demonstrated that differences in the height of these regions, e.g., between BL and SL, form steplike domain boundaries that can serve as pathways for intercalation by locally weakening the carbon-carbon bonding.<sup>20,21</sup> Steps in SiC arising from substrate miscut can give rise to further variations in graphene thickness forming more complex boundaries where intercalation can occur. Efforts to understand the intercalation process at a mechanistic level have focused primarily on ultrahigh vacuum (UHV) methods which provided valuable insights into the role of point defects, domain boundaries, steps, and other nonuniformities

in EG as routes for metal intercalation. <sup>20,21</sup> Due to the pristine conditions employed in UHV, however, these studies have not focused on the impact of chemical functionalization of graphene, particularly functionalization with oxygen that readily occurs when surfaces are plasma-treated and/or exposed to ambient air. Chemical functionalization modifies the electronic structure of graphene altering the energy landscape for adsorption, diffusion, and intercalation. <sup>22</sup> In addition, substantial differences in chemical reactivity are observed for BL, SL, and freestanding graphene. <sup>23</sup> Consequently, variations in EG thickness and reactivity are expected to impact the intercalation process for Ga and N but have not been examined in detail.

In this study, a combined experimental and theoretical approach was used to investigate the effects of defects, thickness nonuniformities, and chemical functionalization of EG on Ga intercalation and 2D-GaN<sub>x</sub> formation to gain insight into this synthesis process. Differences in Ga intercalation and 2D-GaN<sub>x</sub> formation observed experimentally across the sample surface were correlated to localized variations in EG thickness and oxygen functionalization. DFT calculations were used to examine the effects of defects and functionalization on the binding energy of Ga to the surface and its reactivity with NH<sub>3</sub> providing a mechanistic understanding of the intercalation process. Based on these results, the use of thin, oxygenfunctionalized buffer layer EG was found to provide uniform formation of 2D-GaN<sub>x</sub> across the sample surface. The results demonstrate the intricate role of defects and surface chemistry on Ga intercalation and  $2D\text{-}GaN_x$  formation in EG formed on SiC.

#### **RESULTS AND DISCUSSION**

**Defect Engineering of Graphene via Plasma Treatment.** Defect engineering in graphene via  $He/O_2$  plasma treatment has been used to improve the lateral coverage area of  $2D\text{-}GaN_x$  and  $2D\text{-}Ga.^{9,15}$  Plasma-induced defects in graphene serve as gateways for atoms to intercalate to the EG/SiC interface. Briggs et al. reported that  $He/O_2$  plasma treatment yields defective graphene that includes C=O, C-OH, and C-O-C bonds in the graphene lattice. As explained earlier, depending on the EG growth process, the thickness of graphene can vary across the sample surface which can directly

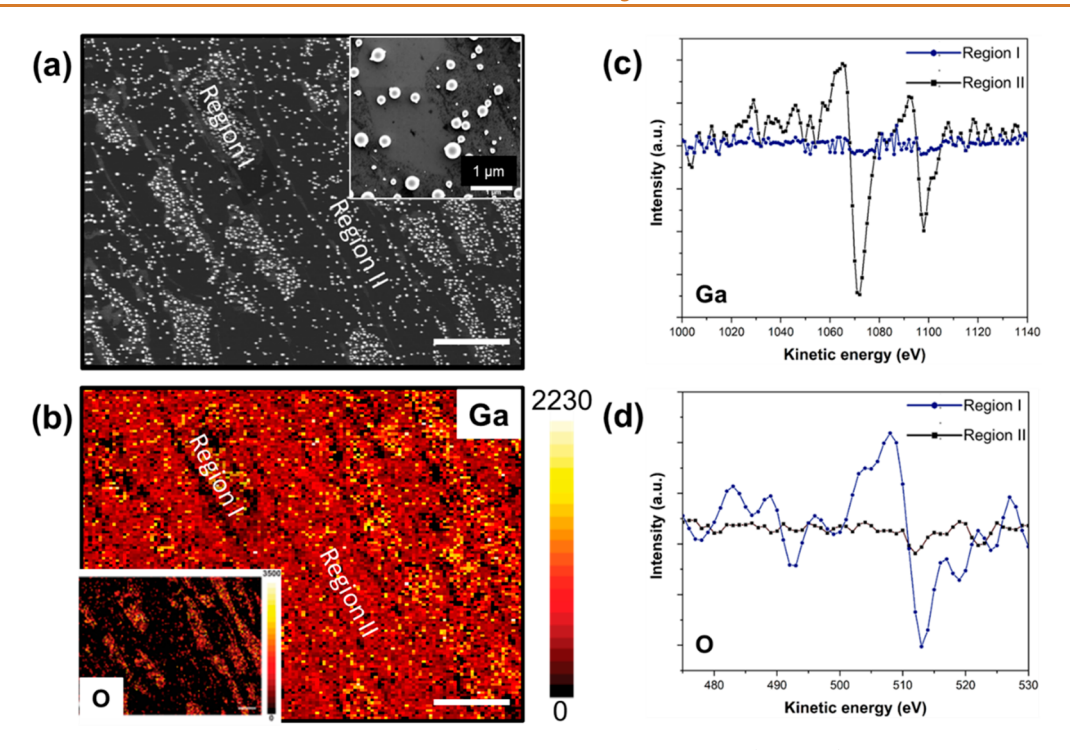


Figure 2. (a) SEM image showing regions of thinner chemically functionalized graphene (region I) that are decorated with Ga droplets compared to thicker EG regions (region II) with few Ga droplets. The inset is a higher-magnification image showing the spherical Ga droplets on the surface of graphene. (b) Ga and O (inset) AES maps of the same region in (a) with bright yellow spots due to the Ga droplets on the surface. Point spectra [dN(E)/d(E)] for Ga (c) and O (d) were obtained in the two areas designated as regions I and II. Region II corresponds to the thicker graphene where there is negligible O and intercalated Ga; region I corresponds to thinner graphene with a distinct O signal and Ga droplets. The scale bar on SEM and AES images is  $10 \mu m$ .

impact its susceptibility toward plasma treatment. Thus, to understand the spatial distribution of functionalized defects, elemental mapping (C, Si, and O) of EG was carried out using Auger electron spectroscopy (AES) pre- and post-plasmatreatment. The samples examined included a nominally bilayer as-grown EG sample and an identical sample that was subjected to 10 s of a  $\rm He/O_2$  plasma (see the Methods section).

Figure 1a shows an SEM micrograph of as-grown EG on SiC. Figure 1b,c shows C and O elemental maps, respectively, from the same area. Based on the contrast in Figure 1a, the sample can be divided into three regions: (i) bright contrast region close to the step edges corresponding to thin/buffer layer EG as can be seen through the low C signal in Figure 1b; (ii) dark contrast region due to thicker EG in the terrace regions of SiC; and (iii) the darkest contrast region which corresponds to the thickest EG at the SiC step edges and exhibits the highest C signal in Figure 1b. As shown in the elemental O map in Figure 1c, thinner EG regions in pristine material show slightly higher O intensity than the surrounding areas indicating chemically defective and reactive graphene in these areas. Figure 1e,f corresponds to Auger maps for C and O, respectively, for plasma-treated EG collected in the area shown in the SEM image in Figure 1d. Similar to the as-grown EG, the carbon signal is highest at the step edges corresponding to the thickest graphene. Regions closer to the step edges are buffer layer/thinner graphene regions represented by reduced C signal from those regions. After plasma treatment, the O signal is significantly higher in the thinner regions of EG when compared to thicker graphene (note the change in z-scale between Figure 1c and Figure 1f), indicating that the C=O and C—OH bonds observed in the X-ray photoelectron spectroscopy (XPS) spectra (Figure S1) correspond to thinner regions of graphene becoming chemically functionalized after the plasma treatment. These results demonstrate that plasma treatment has a pronounced effect specifically on buffer layer regions in the EG resulting in chemically active defects that are not as prevalent on the thicker graphene regions.

Ga Intercalation in Plasma-Treated EG. Intercalation of Ga atoms into plasma-treated EG was investigated to study differences in intercalation between the two main regions of graphene identified in Figure 1: thinner graphene (region I) where plasma treatment results in chemically functionalized defects (C=O, C-OH, and C-O-C) and thicker EG (region II) which is not chemically functionalized. Gallium was intercalated between the plasma-treated EG and SiC by sequential pulsing of TMGa in an MOCVD reactor followed by annealing in H<sub>2</sub> as described in the Methods section. As shown in the SEM image in Figure 2a, Ga droplets decorate the surface in the thinner graphene/O-rich regions (region I) suggesting that the chemical functionalization has altered the properties of the graphene surface. In contrast, in the thicker graphene regions (region II) that did not exhibit functionalization, Ga was found to intercalate between the EG and SiC as shown in the Auger map of Ga in the same region as the SEM image in Figure 2b. Auger point spectra [dN(E)/d(E)] for Ga and O, respectively, shown in Figure 2c,d, further support these results. Note that the Auger point spectra were obtained in areas between the Ga droplets (shown in the inset in Figure 2a) to ascertain the chemistry of the underlying layers. The Ga signal is below the noise in region I (Figure 2c), but oxygen is clearly present (Figure 2d). In contrast, a strong Ga signal is observed in region II (Figure 2c) indicating Ga intercalation in

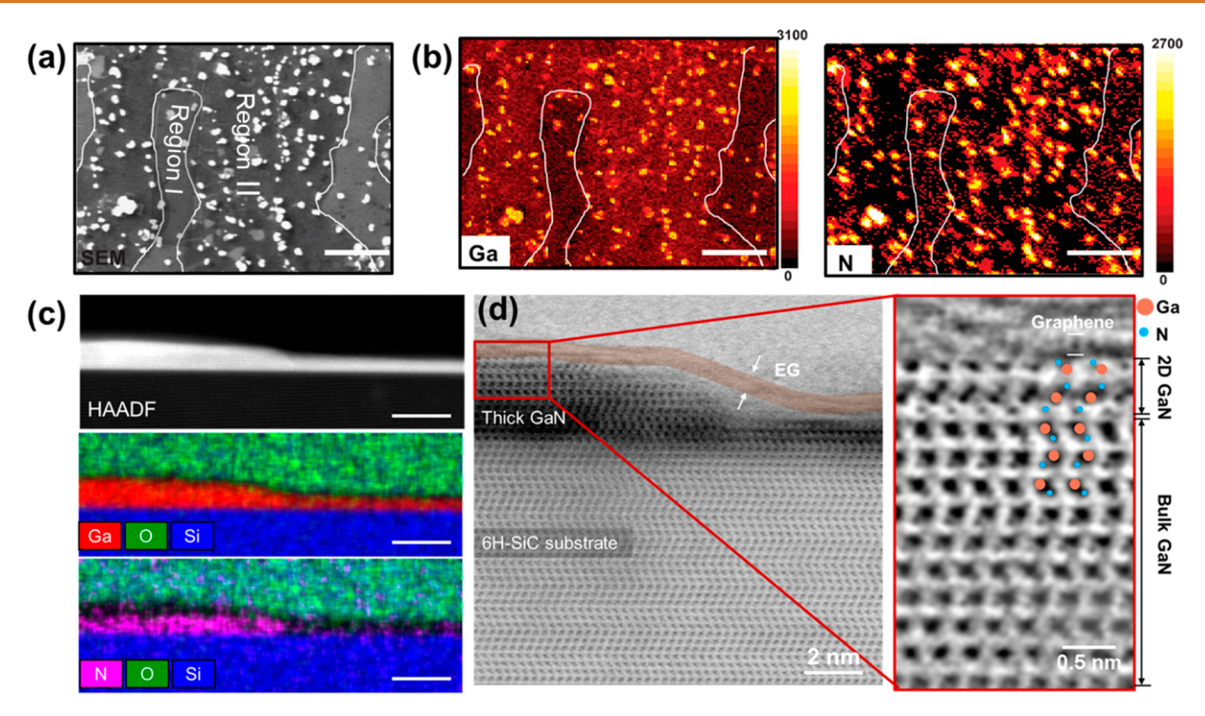


Figure 3. (a) SEM image of sample prepared with the one-step process showing regions of bright contrast that correspond to thinner regions of graphene (region I, outlined in white) and darker contrast regions which correspond to thicker regions of graphene (region II). The white circular features on the image are GaN clusters on the graphene surface. (b) Elemental Ga (left) and N (right) Auger maps corresponding to areas shown in panel a. Ga is detected across the entire surface indicating intercalated Ga while the N signal is enhanced in regions of thinner graphene indicating conversion of intercalated Ga to 2D-GaN<sub>x</sub>. The scale bar for all plots is  $10 \,\mu\text{m}$ . (c) HAADF STEM image and the corresponding EDS maps of a cross-section sample that was obtained at the intersection of regions I and II showing intercalation of Ga and N in the thinner graphene regions and Ga intercalation beneath the thicker graphene. The scale bars for all plots is 7 nm. (d) ABF STEM images showing atomic columns of GaN<sub>x</sub> and Ga intercalated between graphene and SiC with graphene (highlighted in orange) at the top. High-resolution image (right) showing wurtzite GaN beneath a top layer of 2D-GaN<sub>x</sub> adjacent to the graphene with the R3m structure.

Table 1. Calculated Energies (in eV) for  $OH_x$  and  $NH_y$  Functionalization of Graphene (Gr),  $NH_x$  Functionalization of an  $OH_x$ -Doped Graphene, and Binding of a Ga Atom to a Pristine (Prist.) Gr with/without  $OH_x$  and/or  $NH_y$  Doping (x = 0, 1 and y = 0-3)<sup>4</sup>

			V)	to Gr (e	l groups	function	ergy of i	ding en	Bin				
	$\mathrm{NH_{y}}$ binding to $\mathrm{OH_{x}} ext{-doped}$ Gr							NH <sub>y</sub> binding to Gr (y=0,3)				OH <sub>x</sub> binding to Gr(x=0,1)	
NH <sub>3</sub> -	NH <sub>2</sub> -	NH-	CNC-	NH <sub>3</sub> -	NH <sub>2</sub> -	NH-	CNC-	NH <sub>3</sub>	NH <sub>2</sub>	NH	CNC	ОН	COC
ОН	ОН	ОН	ОН	COC	COC	COC	COC						
0.15	2.56	3.45	4.54	2.08	1.52	3.65	5.09	0.15	1.04	3.03	3.82	1.43	3.94
	(eV)	l y=0,3)	=0,1 and	Gr (eV) (x	doped C	nd/or NH	o OH <sub>x</sub> aı	energy t	oinding	Ga l			
	OH <sub>x</sub> and NH <sub>y</sub> -doped Gr (x=0,1 and y=0,2)						NH <sub>y</sub> -doped Gr (y=0,2)				OH <sub>x</sub> -doped Gr (x=0,1)		
Prist.	NH <sub>2</sub> -	ИН-ОН	C- N	- CN	NH <sub>2</sub> ·	NH-	CNC-	$NH_2$	I I	NH	CNC	ОН	COC
	ОН			OH	COC	COC	COC						
1.27	0.60	.55	2 3	4.5	3.78	3.44	2.98	0.29	9 (	2.7	3.73	0.31	3.34

<sup>&</sup>quot;Physisorbed NH<sub>3</sub> on a hydroxylated Gr and NH<sub>3</sub> decomposition to NH<sub>2</sub> via epoxide ring opening are highlighted with a gray background. All binding reactions are exothermic.

these regions, but the O level is below the noise (Figure 2d). The results demonstrate that Ga accumulates on the surface in

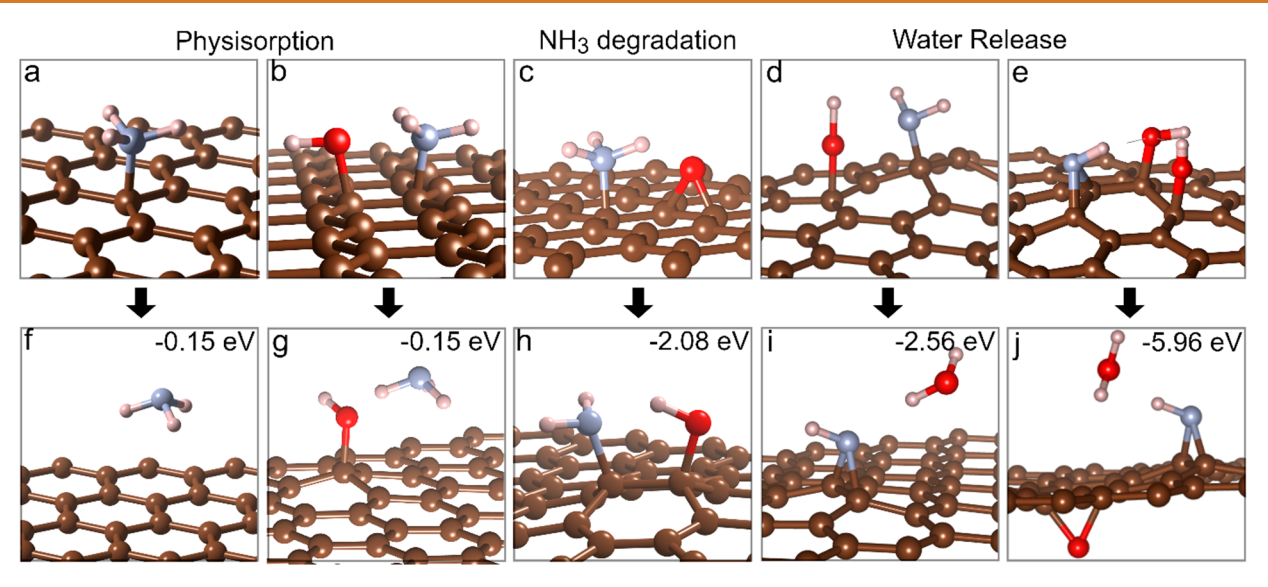


Figure 4. Ball-and-stick illustrations of surface interactions of  $NH_y$  groups with the oxygen-functionalized graphene surface at the DFT level. Brown, blue, red, and white spheres represent carbon, nitrogen, oxygen, and hydrogen atoms, respectively. (a-e) Initial and (f-j) optimized configurations of each model. Physisorption of  $NH_3$  on a (a, f) pristine and (b, g) hydroxylated graphene with a binding energy of -0.15 eV. (c, h)  $NH_3$  decomposition into a surface-bound  $NH_2$  species and  $H_2O$  formation in the proximity of an epoxy group. (d, i)  $NH_2$  decomposition into an NH-surface bound species and  $H_2O$  formation in the proximity of an OH- group. (e, j)  $H_2O$  formation through hydrogen transfer reactions between the OH and NH functional groups.

the thin graphene regions that are functionalized with oxygen suggesting that O-functionalized defects serve as sites for Ga accumulation on the graphene surface and inhibit intercalation.

**2D-GaN<sub>x</sub> Formation.** The synthesis of 2D-GaN<sub>x</sub> was initially attempted using a two-step process, whereby Ga intercalated samples were placed back into the MOCVD reactor, heated in H<sub>2</sub> to 675 °C, and exposed to NH<sub>3</sub> as described in the Methods section. In all cases, however, the Ga deintercalated from the EG as the sample was heated and did not convert to  $GaN_x$  (see the Supporting Information). As a result, a single-step process was employed, similar to the approach of Al Balushi et al.9 whereby Ga intercalation using TMGa was followed immediately by annealing of the sample in NH<sub>3</sub> in the MOCVD reactor. Plasma-treated EG was intercalated with Ga using the same procedure described previously (TMGa pulsing and H<sub>2</sub> annealing at 675 °C), and the sample was immediately exposed to NH<sub>3</sub> at 675 °C. The plasma-treated EG used for this study again consists of the regions of darker and lighter contrast shown in Figures 1 and 2. SEM and Auger mapping were used to characterize the sample surface. As shown in Figure 3a, following NH<sub>3</sub> annealing at 675 °C, the thinner graphene (region I) undergoes 2D-GaN<sub>x</sub> intercalation; however, the thicker regions (region II) with intercalated Ga did not convert to GaN<sub>x</sub> as seen through the SEM image in Figure 3a and the Auger maps for Ga and N postannealing in Figure 3b.

To investigate the intercalated material further, a cross-section sample was prepared using a focused ion beam (FIB) to select a region that included both thinner and thicker graphene. Energy dispersive spectroscopy (EDS) carried out in a scanning transmission electron microscope (STEM) was used to chemically analyze the sample as shown in Figure 3c. As can be seen from the EDS maps, Ga is present along the entire interface between the EG and SiC; however, nitrogen was primarily observed in regions with a thicker Ga layer which corresponds to the thinner graphene (region I) shown in Figure 3a. To confirm the crystal structure of 2D-GaN<sub>x</sub>,

annular bright-field (ABF) STEM images were collected (Figure 3d). The left side of the image contains the region of thicker Ga where N is also present; a magnified image of this region (rightmost image in Figure 3d) shows that the majority of the intercalated Ga and N are present as wurtzite (P63mc) GaN. However, the topmost layer closest to the graphene has the rhombohedral (R3m) structure, similar to the structure reported previously by Al Balushi et al. Adjacent to the 2D-GaN<sub>x</sub>/GaN region in Figure 3d is a region where Ga only intercalated; this area corresponds to the thicker graphene that has a darker contrast in Figure 3a. Graphene was observed to cover both the 2D-GaN<sub>x</sub>/GaN and 2D-Ga regions (highlighted region in Figure 3d); however, it is difficult to identify the exact number of graphene layers on the 2D-GaN<sub>x</sub>/GaN vs 2D-Ga from the ABF-STEM images.

DFT calculations were performed to evaluate  $NH_y$  (y = 1-3) interactions with oxidized regions of graphene and to explain the experimental results. According to the DFT results displayed in Table 1, oxygen-containing functional groups (i.e., C-OH and C-O-C) on graphene facilitate  $NH_3$  dissociation to its derivatives since the NH, species display a higher binding energy to oxidized graphene than to bare graphene, in line with previous work.<sup>24</sup> This indicates a catalytic role of surface oxygen sites in NH, binding, aligned with the experimental observations (Figure 3b). Note that the physisorption of NH<sub>3</sub> on a hydroxylated pristine graphene surface occurs through van der Waals interactions and weak H<sub>2</sub>N-H···OH hydrogen bonds (Figure 4a), which is followed by thermodynamically favored H-transfer from NH<sub>x</sub> to OH<sub>x</sub> groups (Figure 4b,d). For example, H-abstraction from N functional groups leads to either the saturation of the epoxy group by the ring opening (Figure 4b) or the removal of OH groups from the surface as H<sub>2</sub>O (Figure 4c,d). This means that the O-rich surface facilitates NH3 decomposition into graphene-bound nitrogen species (i.e., NH-, NH<sub>2</sub>, and N-) and enhances the concentration of active sites (i.e., NH- and N-) on the

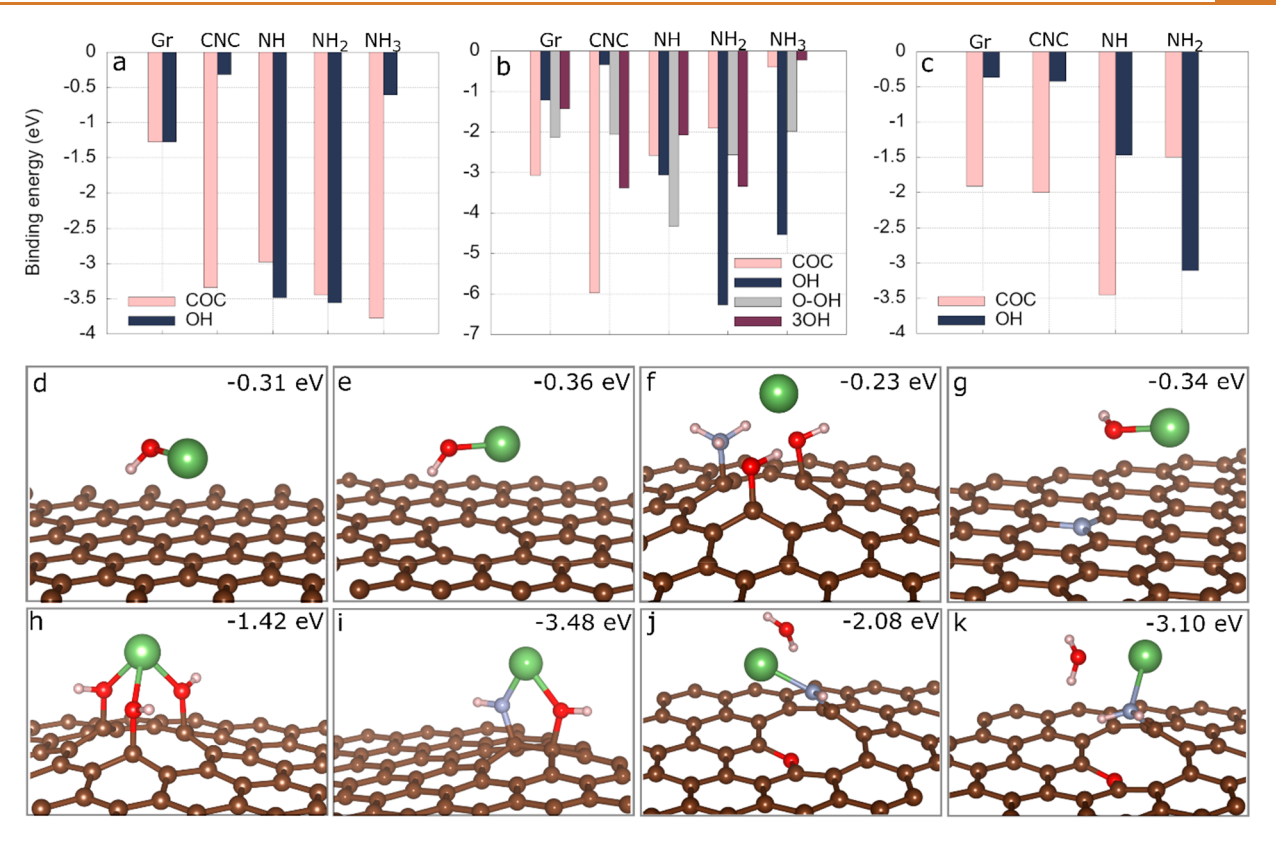


Figure 5. Calculated binding energies of Ga on (a) pristine, (b) SV, and (c) DV oxygen-functionalized graphene (Gr) with/without N-containing functional groups. Ball-and-stick illustration and energies of Ga adsorption on representative  $OH_x$ -functionalized graphene without (d, e, h) and with (f, g, i, k) NH<sub>y</sub> doping. Green, red, white, blue, and brown spheres represent gallium, oxygen, hydrogen, nitrogen, and carbon atoms, respectively. Pristine surface without (d) and with (i) an NH– group. SV model with three OH– (h) and an NH– and two OH– groups (j). DV model with an OH– (e) and two OH– and NH<sub>2</sub> groups (k). Physisorption of Ga to (f) NH<sub>3</sub> and (g) graphitic N-doped oxygen-functionalized graphene with an SV defect. The graphene surface contains (f) two OH– and one NH<sub>3</sub> and (g) one OH– and one graphitic N group.

surface (Figure 4c,d) which, in turn, can initiate the formation of  $2D\text{-GaN}_x$ .

The experimental results demonstrate that, in the region of thinner, oxygen-functionalized graphene, Ga only intercalates in the presence of NH<sub>3</sub> leading to the formation of 2D-GaN<sub>x</sub>. Gallium does not intercalate in thinner graphene regions except when it is carried out in conjunction with NH<sub>3</sub> annealing in the same reactor without air exposure in between the steps. Therefore, comparative DFT studies were further performed to examine the adsorption of Ga metal on pristine and OH<sub>x</sub>-functionalized graphene surfaces with and without Ncontaining functional groups. Epoxy and OH functional groups were introduced first in three representative models: pristine graphene and oxygen-functionalized graphene with a single vacancy (SV) and a divacancy (DV). After structural relaxation, the oxygen-functionalized graphene was doped further with NH<sub> $\nu$ </sub> ( $\nu = 0-3$ ), followed by a second structural relaxation. Subsequently, a Ga atom was anchored on each graphene sheet.

Figure 5 compares the adsorption energies of a Ga atom on oxygen-functionalized graphene with and without N-containing functional groups. In the absence of NH<sub>y</sub>, functionalization, the Ga-binding strength to the epoxy (C-O-C) group is stronger (-3.34 eV) than that to the bare basal plane (-1.27 eV) (Figure 5a). On the other hand, the hydroxylated (OH) regions significantly weaken the binding strength of the Ga atom to graphene, resulting in a lower binding energy (-0.31 eV) (Figure 5a,d) than even that of the basal plane. Even in the

presence of a single vacancy and a divacancy, oxygen functionalization does not help attract Ga atoms toward the surface of graphene as seen through the binding energy calculations in Figure 5b,c,e. This indicates that the hydroxyl terminations are unlikely to attract Ga atoms to the surface, as also observed in the experiments where Ga does not intercalate in oxygen-functionalized thinner graphene regions (Figure 2) in the absence of NH<sub>3</sub>. Additionally, because of the absence of surface dangling bonds, the Ga binding strength to the NH<sub>3</sub> (e.g., -0.23 eV for SV in Figure 5f, Table 1) and graphitic-Ndoped OH-regions (e.g., -0.34 eV for SV in Figure 5g, Table 1) are significantly weaker even than that of the nonfunctionalized pristine graphene -1.27 eV (Table 1), indicating that the physisorption of Ga on NH3-functionalized hydroxylated graphene occurs through weak interactions. The surface interactions of Ga with a graphitic-N-doped defective graphene may also lead to the formation of Ga(OH), adduct (Figure 5g). On the other hand, as displayed in Table 1 and depicted in Figure 5a-c,i-k, the introduction of an NH<sub>v</sub> (N-, NH-, and NH<sub>2</sub>-) group in oxidized graphene significantly enhances the Ga-binding ability of graphene, inducing the chemisorption of Ga metals on the surface through covalent bonds, in line with the experimental observations.

All these results together signify that the NH- and NH<sub>2</sub>-species are expected to dominate the oxidized surface due to the surface recombination reactions with -OH species, and these species provide strong binding sites for Ga atoms and thus can serve as a coupling agent between the oxidized

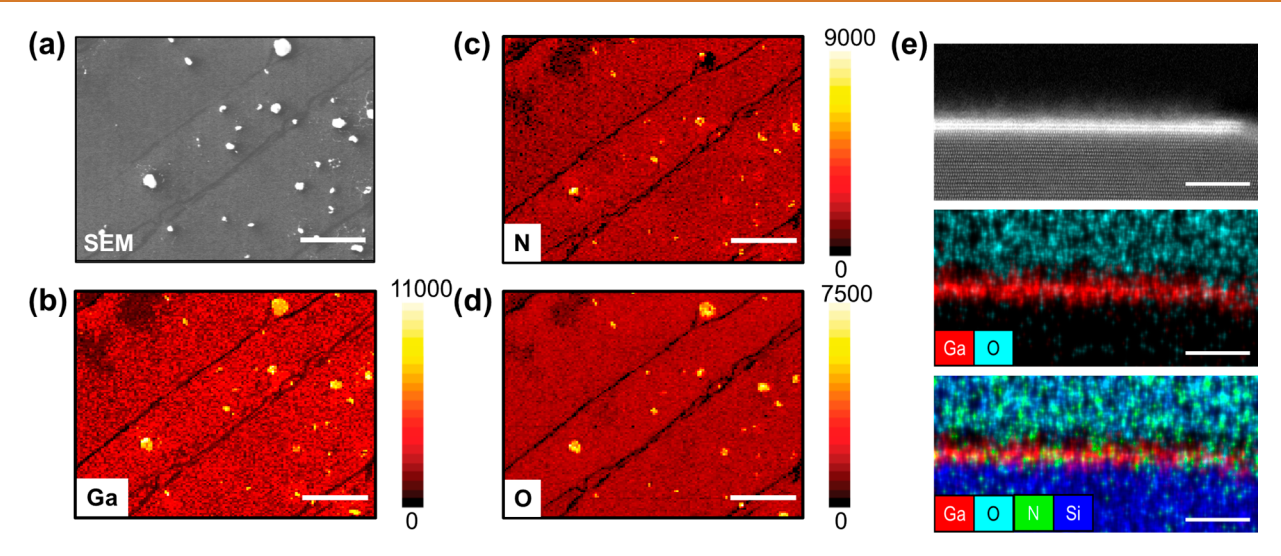


Figure 6. (a) SEM image of a buffer layer EG sample prepared with a one-step process showing a relatively uniform contrast across the entire surface (white circular features are GaN clusters on the surface, and dark lines are step edges). (b, c, d) Ga,N, and O elemental maps showing large area coverage of GaN on buffer layer EG samples. The scale bar on SEM and AES images is 10  $\mu$ m. (e) HAADF-STEM cross-section of sample showing a region of bright contrast at the graphene/SiC interface. Elemental EDS maps of Ga, O, N, and Si showing the presence of both Ga and N at the graphene/SiC interface. The scale bar on the TEM images is 7 nm.

graphene and metal atoms (Figure 5). Whereas, in the absence of NH— and NH $_2$  species, Ga weakly interacts with hydroxylated graphene. This is in line with the experimental observations reported in this study where, in absence of NH $_3$  annealing, Ga does not intercalate in regions of oxygenfunctionalized thinner graphene whereas as soon as the NH $_3$  annealing step is introduced, 2D-GaN $_x$  formation takes place between graphene and SiC. It should be noted that experiments were carried out in which the NH $_3$  annealing step was performed first before TMGa exposure; in this case 2D-GaN $_x$  did not form. This suggests that although Ga weakly interacts with the hydroxylated graphene, it is necessary to have some Ga on the graphene surface prior to annealing in NH $_3$  for GaN $_x$  to intercalate.

2D-GaN<sub>x</sub> Intercalation Using Buffer Layer EG. The previous results demonstrate that thinner regions of graphene chemically functionalized with oxygen are favorable for the formation of 2D-GaN<sub>x</sub> between graphene and SiC. Therefore, to synthesize large areas of 2D-GaN<sub>r</sub> between graphene and SiC, an EG sample consisting of primarily buffer layer EG was employed as the substrate (see the Methods section). Figure S6 shows the (a) Raman spectra and (b) XPS spectra of the asgrown buffer layer EG before intercalation. The absence of a 2D peak at 2700 cm<sup>-1</sup> in the Raman spectra indicates the absence of freestanding graphene layers on top of the buffer layer. Moreover, the D peak in the Raman spectra and presence of C-OH and C=O peaks in the C 1s spectra indicate high defect density in the buffer layer EG. Due to the presence of oxygen on the as-grown buffer layer surface, the buffer layer EG samples were not plasma-treated prior to the intercalation. The one-step process described in the previous section was used for Ga intercalation and NH3 annealing as described in the Methods section. The SEM image (Figure 6a) shows more uniform contrast across the entire surface, and Auger maps of Ga and N (Figure 6b,c) indicate that intercalated GaN<sub>x</sub> was obtained throughout the sample. In addition, O was also observed uniformly across the sample (Figure 6d). This might be due to oxygen functionalization of the defective as-grown buffer layer EG or physisorbed oxygen

on the surface due to N doping in the graphene as previously reported in the literature. A high-angle annular dark-field (HAADF)-STEM image and the corresponding EDS maps of the sample cross-section (Figure 6e) suggest that there are  $\sim 2-3$  layers of Ga in the form of  $\operatorname{GaN}_x$  or a complex of  $\operatorname{GaN}_x O_y$  between the graphene and SiC given that ultrathin  $\operatorname{Ga}_2 O_3$  exhibits a similar R3m structure. ABF STEM imaging was attempted on the sample to obtain a high-resolution image similar to Figure 3d; however, the atomic resolution was poor, and consequently, it was not possible to identify the crystal structure of the intercalated layers. Nevertheless, the results demonstrate that buffer EG is a promising template to obtain large area 2D-GaN<sub>x</sub> for future studies.

# **CONCLUSIONS**

A combined experimental and theoretical approach was used to investigate the effects of defects, thickness nonuniformities, and chemical functionalization of epitaxial graphene (EG) formed on SiC on Ga intercalation and 2D-GaN<sub>x</sub> formation to gain insight into this synthesis process. A He/O2 plasma was used to introduce oxygen-functionalized defects in the EG which preferentially formed in thin buffer layer regions on the surface. The oxygen functionalization inhibited Ga intercalation but led to 2D-GaN<sub>x</sub> formation when the sample was immediately annealed in NH3. In contrast, Ga intercalated in the regions that were not oxygen-functionalized but did not convert to 2D-GaN, leading to a mixture of intercalated Ga and 2D-GaN<sub>x</sub> at the EG/SiC interface. Density functional theory (DFT) calculations reveal the role of surface functionalization on the intercalation process. Oxygen functionalization of graphene in the form of hydroxyl groups reduces the binding energy of Ga to the surface decreasing the likelihood of intercalation. However, the hydroxyl groups enhance the reactivity of the graphene surface toward NH3 leading to NHx functionalization which, in turn, facilitates the binding of Ga to the surface and 2D-GaN<sub>x</sub> formation. The use of an oxygen-functionalized epitaxial graphene buffer layer resulted in uniform 2D-GaN<sub>x</sub> intercalation across the entire sample surface. The results demonstrate the intricate role of

defects and surface chemistry on Ga intercalation and 2D-GaN, formation in EG formed on SiC.

#### **METHODS**

**Epitaxial Growth of Graphene.** EG was synthesized via sublimation of silicon from the Si-side of a semi-insulating 6H-SiC (II–VI Incorporated) surface. First, the samples were etched in a mixture of an Ar (450 sccm) and  $H_2$  (50 sccm) gas environment at 1500 °C and 700 Torr for 30 min to remove damages from surface polishing. Then, graphene epitaxy was achieved by annealing the samples under Ar (500 sccm) at 1800 °C and 700 Torr for 20 min. Prior to the growth, 6H-SiC substrates were cleaned with acetone (10 min) and isopropyl alcohol (10 min) and rinsed with deionized (DI) water.

**MOCVD of 2D-Ga/2D-GaN**<sub>x</sub>. A vertical cold wall showerhead reactor with RF inductive heating was used for MOCVD growth of 2D-Ga and 2D-GaN. For 2D-Ga growths, samples were held at 550 °C in 8.1 slm total flow of H<sub>2</sub> under a pressure of 100 Torr. 100 cycles of 8.93  $\mu$ mol min<sup>-1</sup> TMGa were pulsed followed by annealing for 10 min at 675 °C. Each cycle consisted of a 2 s pulse of TMGa and a 3 s purge in hydrogen. For converting intercalated Ga into GaN, intercalated Ga samples were annealed in an ultra-high-purity NH<sub>3</sub> environment (62.5 mmol min<sup>-1</sup>) at 675 °C for 30 min at a reactor pressure of 100 Torr. Samples were ramped to 675 °C and held for 5 min.

Plasma Treatment of Epitaxial Graphene. Epitaxial graphene layers were plasma-treated using a Tepla M4L plasma etch tool, using 150 sccm  $O_2$  and 50 sccm under a pressure of 500 mTorr and power of 50 W.

**Raman Spectroscopy.** A Horiba LabRam Raman system using a wavelength of 488 nm and a power of 5 mW was used to collect Raman spectra. Spectra are acquired with an integration time of 2 min, using a 600 grooves/mm grating. As measured, the Raman spectra contain peaks associated with epitaxial graphene (EG) and SiC. To remove the SiC peaks, the Raman spectrum of the underlying SiC was collected by focusing 50  $\mu$ m below the sample surface. The background SiC spectrum was then subtracted from the EG + SiC spectrum to obtain the EG Raman spectrum.

Scanning Electron Microscopy. For FESEM images of as-grown and intercalated EG samples, a Zeiss Merlin instrument with an accelerating voltage of 10 keV was used.

**X-ray Photoelectron Spectroscopy.** X-ray photoelectron spectroscopy measurements were carried out with a Physical Electronics Versa Probe II instrument equipped with a monochromatic Al K $\alpha$  X-ray source ( $h\nu=1486.7$  eV) and a concentric hemispherical analyzer. High-resolution spectra were obtained over an analysis area of 200  $\mu$ m at a pass energy of 29.35 eV for C 1s, Si 2p, Ga 3d, and Ga 2p regions. O 1s regions were collected with a pass energy of 46.95 eV. The spectra were charge referenced to this graphene peak in C 1s corresponding to 284.5 eV. U 2 Tougaard background was used for peak fitting.

**Auger Electron Spectroscopy.** Elemental mapping via Auger electron spectroscopy was conducted using a Physical Electronics (PHI) model 670 scanning Auger system with field-emitter. Voltage and beam current used for the mapping were 10 keV and 10 nA, respectively. An integration time of 0.1 s (per pixel) with 1 eV steps was used. For image quality, 3 frames are averaged for C maps, while 10 frames are averaged for Ga, Si, and O maps. A 2-point acquisition method was used for the intensity calculation at each point with the following peak/background energy values used for each of the following elements: (Ga) 1068.0/1080.0 eV, (N, C) 267.7/291.0 eV, (O) 509.3/532.0 eV, and (Si) 1612.5/1630.0 eV.

**Transmission Electron Microscopy.** Cross-section TEM samples were prepared by in situ lift-out via milling in an FEI Helios NanoLab DualBeam 660 focused ion beam (FIB). Prior to FIB, roughly 60/5/10 nm of SiO<sub>2</sub>/Ti/Au was deposited via electron beam evaporation in a Kurt J. Lesker Lab18 evaporator, to improve contrast during STEM imaging at low magnifications. Contrast was improved by increasing the separation distance between the graphene/Ga/SiC

interface of interest and the bright conductive layers deposited on the sample surface during FIB. Samples were cross-sectioned with a  $\rm Ga^+$  ion beam at 30 kV and then stepped down to 1 kV to avoid ion beam damage to the sample surface. High-resolution scanning transmission electron microscopy (HR-STEM) was conducted in a double aberration-corrected FEI Titan3 G2 60–300 kV STEM at 200 kV. The annular bright-field (ABF) images were collected using an FEI DF4 detector. The collection angle was 7–40 mrad with a 115 mm camera length. EDS mapping was conducted using the SuperX EDS system under STEM mode.

VASP Calculations. Density functional theory (DFT) calculations were performed using the Vienna ab initio simulation package (VASP).1 The electron-ionic core relation was represented using a Projected Augmented Potential, 2,3 in combination with the generalized gradient approximations of Perdew-Burke-Ernzerhof<sup>4,5</sup> to treat exchange-correlation interactions. A Monkhorst—Pack k-point mesh of  $6 \times 6 \times 1$  was employed for a graphene sheet with the size of  $14.786 \times 14.786 \text{ A}^2$  to sample the Brillouin zone. The convergence criteria of energy and force were set to 0.1 meV and 0.01 eV/Å with a plane-wave expansion energy cutoff of 500 eV. Gaussian broadening of width 0.05 eV was used; the dispersion corrections were incorporated into the DFT calculations using the zero damping DFT-D3 method<sup>6</sup> to account for van der Waals interactions. A vacuum layer of 20 Å was inserted normal to the graphene sheet to minimize the extent of the spurious interactions between replicas. Three representative models were adopted for the graphene sheet: pristine, single vacancy (SV), and divacancy (DV) defect models for which one and two atoms were detached from the center of a pristine graphene, respectively.

#### ASSOCIATED CONTENT

# Supporting Information

The Supporting Information is available free of charge at https://pubs.acs.org/doi/10.1021/acsnano.2c07091.

Additional data and figures including XPS spectra; plots of SiC C 1s peak position and  $\delta$ ; SEM image; AES maps; and Raman spectra (PDF)

#### **AUTHOR INFORMATION**

#### **Corresponding Author**

Joan M. Redwing — Department of Materials Science and Engineering and 2-Dimensional Crystal Consortium Materials Innovation Platform (2DCC-MIP) Materials Research Institute, The Pennsylvania State University, University Park, Pennsylvania 16802, United States; orcid.org/0000-0002-7906-452X; Email: jmr31@psu.edu

### Authors

Anushka Bansal — Department of Materials Science and Engineering, The Pennsylvania State University, University Park, Pennsylvania 16802, United States; orcid.org/0000-0003-4340-362X

Nadire Nayir — Department of Physics, Karamanoglu Mehmetbey University, Karaman 70000, Turkey; 2-Dimensional Crystal Consortium Materials Innovation Platform (2DCC-MIP) Materials Research Institute and Department of Mechanical Engineering, The Pennsylvania State University, University Park, Pennsylvania 16802, United States; orcid.org/0000-0002-3621-2481

Ke Wang — Materials Characterization Laboratory, Materials Research Institute, The Pennsylvania State University, University Park, Pennsylvania 16802, United States

- Patrick Rondomanski Department of Materials Science and Engineering, The Pennsylvania State University, University Park, Pennsylvania 16802, United States
- Shruti Subramanian Department of Materials Science and Engineering, The Pennsylvania State University, University Park, Pennsylvania 16802, United States; orcid.org/0000-0002-8933-9486
- Shalini Kumari Department of Materials Science and Engineering, The Pennsylvania State University, University Park, Pennsylvania 16802, United States
- Joshua A. Robinson Department of Materials Science and Engineering and 2-Dimensional Crystal Consortium Materials Innovation Platform (2DCC-MIP) Materials Research Institute, The Pennsylvania State University, University Park, Pennsylvania 16802, United States;

  orcid.org/0000-0002-1513-7187
- Adri C. T. van Duin 2-Dimensional Crystal Consortium Materials Innovation Platform (2DCC-MIP) Materials Research Institute and Department of Mechanical Engineering, The Pennsylvania State University, University Park, Pennsylvania 16802, United States; orcid.org/0000-0002-3478-4945

Complete contact information is available at: https://pubs.acs.org/10.1021/acsnano.2c07091

#### **Author Contributions**

The manuscript was written through the contributions of all authors. All authors have approved the final version of the manuscript. A.B. carried out the sample preparation (plasma treatment and MOCVD growth), characterization (Raman/PL spectroscopy, XPS spectroscopy, and Auger spectroscopy), and data analysis. N.N. carried out the DFT calculations. K.W. conducted the STEM/EDS analysis. P.R. carried out the FESEM characterization. S.S. and S.K. synthesized the EG/SiC samples for the study. A.B., N.N., K.W., P.R., S.S., S.K., J.A.R., A.C.T.v.D., and J.M.R. discussed the results. The work was conceived and supervised by J.A.R., A.C.T.v.D., and J.M.R.

#### Notes

The authors declare no competing financial interest.

#### **ACKNOWLEDGMENTS**

Financial support was provided by the National Science Foundation through DMR-1808900 and the 2D Crystal Consortium—Materials Innovation Platform (2DCC-MIP) at The Pennsylvania State University under NSF cooperative agreements DMR-1539916 and DMR-2039351. We thank H. Wang for TEM sample preparation using FIB. All microscopy work was performed at the Penn State Materials Characterization Laboratory.

# **REFERENCES**

- (1) Bhimanapati, G. R.; Lin, Z.; Meunier, V.; Jung, Y.; Cha, J.; Das, S.; Xiao, D.; Son, Y.; Strano, M. S.; Cooper, V. R.; Liang, L.; Louie, S. G.; Ringe, E.; Zhou, W.; Kim, S. S.; Naik, R. R.; Sumpter, B. G.; Terrones, H.; Xia, F.; Wang, Y.; Zhu, J.; Akinwande, D.; Alem, N.; Schuller, J. A.; Schaak, R. E.; Terrones, M.; Robinson, J. A. Recent Advances in Two-Dimensional Materials beyond Graphene. *ACS Nano* 2015, *9*, 11509–11539.
- (2) Briggs, N.; Subramanian, S.; Lin, Z.; Li, X.; Zhang, X.; Zhang, K.; Xiao, K.; Geohegan, D.; Wallace, R.; Chen, L. Q.; Terrones, M.; Ebrahimi, A.; Das, S.; Redwing, J.; Hinkle, C.; Momeni, K.; Van Duin, A.; Crespi, V.; Kar, S.; Robinson, J. A. A Roadmap for Electronic Grade 2D Materials. 2D Materials 2019, 6, No. 022001.

- (3) Das, S.; Robinson, J. A.; Dubey, M.; Terrones, H.; Terrones, M. Beyond Graphene: Progress in Novel Two-Dimensional Materials and van Der Waals Solids. *Annu. Rev. Mater. Res.* **2015**, 45, 1–27.
- (4) Zhuang, H. L.; Singh, A. K.; Hennig, R. G. Computational Discovery of Single-Layer III-V Materials. *Phys. Rev. B* **2013**, *87*, 165415.
- (5) Singh, A. K.; Zhuang, H. L.; Hennig, R. G. Ab Initio Synthesis of Single-Layer III-V Materials. *Phys. Rev. B* **2014**, *89*, 245431.
- (6) Singh, A. K.; Hennig, R. G. Computational Synthesis of Single-Layer GaN on Refractory Materials. *Appl. Phys. Lett.* **2014**, *105*, No. 051604.
- (7) Freeman, C. L.; Claeyssens, F.; Allan, N. L.; Harding, J. H. Graphitic Nanofilms as Precursors to Wurtzite Films: Theory. *Phys. Rev. Lett.* **2006**, *96*, No. 066102.
- (8) Tasker, P. W. The Stability of Ionic Crystal Surfaces. J. Phys. C Solid State Phys. 1979, 12, 4977-4984.
- (9) Al Balushi, Z. Y.; Wang, K.; Ghosh, R. K.; Vilá, R. A.; Eichfeld, S. M.; Caldwell, J. D.; Qin, X.; Lin, Y.-C.; DeSario, P. A.; Stone, G.; Subramanian, S.; Paul, D. F.; Wallace, R. M.; Datta, S.; Redwing, J. M.; Robinson, J. A. Two-Dimensional Gallium Nitride Realized via Graphene Encapsulation. *Nat. Mater.* **2016**, *15*, 1166–1171.
- (10) Huang, W.; Gan, L.; Li, H.; Ma, Y.; Zhai, T. 2D Layered Group IIIA Metal Chalcogenides: Synthesis, Properties and Applications in Electronics and Optoelectronics. *CrystEngComm* **2016**, *18*, 3968–3984.
- (11) Wang, W.; Zheng, Y.; Li, X.; Li, Y.; Zhao, H.; Huang, L.; Yang, Z.; Zhang, X.; Li, G. 2D AlN Layers Sandwiched Between Graphene and Si Substrates. *Adv. Mater.* **2019**, *31*, 1803448.
- (12) Wang, W.; Li, Y.; Zheng, Y.; Li, X.; Huang, L.; Li, G. Lattice Structure and Bandgap Control of 2D GaN Grown on Graphene/Si Heterostructures. *Small* **2019**, *15*, 1802995.
- (13) Pécz, B.; Nicotra, G.; Giannazzo, F.; Yakimova, R.; Koos, A.; Kakanakova-Georgieva, A. Indium Nitride at the 2D Limit. *Adv. Mater.* **2021**, 33, 2006660.
- (14) Nisi, K.; Subramanian, S.; He, W.; Ulman, K. A.; El-Sherif, H.; Sigger, F.; Lassaunière, M.; Wetherington, M. T.; Briggs, N.; Gray, J. Light—Matter Interaction in Quantum Confined 2D Polar Metals. *Adv. Funct. Mater.* **2021**, *31*, 2005977.
- (15) Briggs, N.; Bersch, B.; Wang, Y.; Jiang, J.; Koch, R. J.; Nayir, N.; Wang, K.; Kolmer, M.; Ko, W.; De La Fuente Duran, A.; Subramanian, S.; Dong, C.; Shallenberger, J.; Fu, M.; Zou, Q.; Chuang, Y.-W.; Gai, Z.; Li, A.-P.; Bostwick, A.; Jozwiak, C.; Chang, C.-Z.; Rotenberg, E.; Zhu, J.; van Duin, A. C. T.; Crespi, V.; Robinson, J. A. Atomically Thin Half-van Der Waals Metals Enabled by Confinement Heteroepitaxy. *Nat. Mater.* **2020**, *19*, 637–643.
- (16) Steves, M. A.; Wang, Y.; Briggs, N.; Zhao, T.; El-Sherif, H.; Bersch, B. M.; Subramanian, S.; Dong, C.; Bowen, T.; Fuente Duran, A. D. La. Unexpected Near-Infrared to Visible Nonlinear Optical Properties from 2-D Polar Metals. *Nano Lett.* **2020**, *20*, 8312–8318. (17) Nayir, N. Density Functional Study of Ga Intercalation at
- Graphene/SiC Heterointerface. J. Mater. Res. 2022, 37, 1172–1182.
- (18) Nayir, N.; Sengul, M. Y.; Costine, A. L.; Reinke, P.; Rajabpour, S.; Bansal, A.; Kozhakhmetov, A.; Robinson, J.; Redwing, J. M.; van Duin, A. Atomic-Scale Probing of Defect-Assisted Ga Intercalation through Graphene Using ReaxFF Molecular Dynamics Simulations. *Carbon N. Y.* **2022**, *190*, 276–290.
- (19) Emtsev, K. V.; Bostwick, A.; Horn, K.; Jobst, J.; Kellogg, G. L.; Ley, L.; McChesney, J. L.; Ohta, T.; Reshanov, S. A.; Roehrl, J.; Rotenberg, E.; Schmid, A. K.; Waldmann, D.; Weber, H. B.; Seyller, T. Towards Wafer-Size Graphene Layers by Atmospheric Pressure Graphitization of Silicon Carbide. *Nat. Mater.* 2009, *8*, 203–207.
- (20) de Jong, T. A.; Kraskovskii, E. E.; Ott, C.; Tromp, R. M.; van der Molen, S. J.; Jobst, J. Intrinsic stacking domains in graphene on silicon carbide: A pathway for intercalation. *Phys. Rev. Mater.* **2018**, *2*, 104005.
- (21) Chen, S.; Theil, P. A.; Conrad, E.; Tringides, M. C. Growth and stability of Pb intercalated phases under graphene on SiC. *Phys. Rev. Mater.* **2020**, *4*, 124005.

- (22) Yamamoto, S.; Takeuchi, K.; Hamamoto, Y.; Liu, R. Y.; Shiozawa, Y.; Koitaya, T.; Someya, T.; Tashima, K.; Fukidome, H.; Mukai, K.; Yoshimoto, S.; Suemitsu, M.; Morikawa, Y.; Yoshinobu, J.; Matsuda, I. Enhancement of CO2 adsoprtion on oxygen-functionalized epitaxial graphene surface under near-ambient conditions. Phys. Chem. Chem. Phys. 2018, 20, 19532.
- (23) Bottari, G.; Angeles Herranz, M.; Wibmer, L.; Volland, M.; Rodriquez-Perez, L.; Guldi, D. M.; Hirsch, A.; Martin, N.; D'Souza, F.; Torres, T. Chemical functionalization and characterization of graphene-based materials. Chem. Soc. Rev. 2017, 46, 4464.
- (24) Tang, S.; Cao, Z. Adsorption and Dissociation of Ammonia on Graphene Oxides: A First-Principles Study. J. Phys. Chem. C 2012, 116, 8778-8791.
- (25) Wei, D.; Liu, Y.; Wang, Y.; Zhang, H.; Huang, L.; Yu, G. Synthesis of N-Doped Graphene by Chemical Vapor Deposition and Its Electrical Properties. Nano Lett. 2009, 9, 1752-1758.
- (26) Dycus, J. H.; Mirrielees, K. J.; Grimley, E. D.; Kirste, R.; Mita, S.; Sitar, Z.; Collazo, R.; Irving, D. L.; LeBeau, J. M. Structure of ultrathin native oxides on III-nitride surfaces. ACS Appl. Mater. Interfaces 2018, 10, 10607-10611.

# **Recommended by ACS**

**Layer-Dependent Magnetic Structure and Anomalous Hall** Effect in the Magnetic Topological Insulator MnBi<sub>4</sub>Te<sub>7</sub>

Jianhua Cui, Xianhui Chen, et al.

FFRRUARY 15, 2023 NANO I FTTERS

READ 2

Real-Space Observation of Ripple-Induced Symmetry Crossover in Ultrathin MnPS<sub>3</sub>

Ziqian Wang, Naoki Ogawa, et al.

JANUARY 26, 2023 ACS NANO

READ **C** 

Electron-Beam- and Thermal-Annealing-Induced Structural Transformations in Few-Layer MnPS,

Alexander Storm, Ute Kaiser, et al.

FEBRUARY 20, 2023

ACS NANO

READ **C** 

Near-Infrared Phototheranostic Iron Pyrite Nanocrystals Simultaneously Induce Dual Cell Death Pathways via **Enhanced Fenton Reactions in Triple-Negative Breast Ca...** 

Chunhua Zhao, Jiang Yang, et al.

JANUARY 27, 2023

ACS NANO

READ **C** 

Get More Suggestions >